

On the source of dense outflows from T Tauri Stars. and III. Winds driven from the star-disc shear layer.

Ana I. Gómez de Castro^{1*} and Brigitta von Rekowski²

¹*S.D. Astronomía y Geodesia, Fac. de CC. Matemáticas, Universidad Complutense de Madrid, Plaza de Ciencias 3, 28040 Madrid, Spain*

²*Institute of Human Genetics, Newcastle University, International Centre for Life, Newcastle upon Tyne NE1 3BZ, UK*

Submitted December 7th, 2009

ABSTRACT

Ultraviolet observations of classical T Tauri Stars (cTTSSs) have shown that there is a hot ($T_e \simeq 80,000$ K) and dense ($n_e \simeq 10^{10}$ cm⁻³) component associated with the large scale jet. This hot component is formed very close to the base of the jet providing fundamental information on the jet formation mechanism. In this series, we have investigated whether this component can be formed in disc winds, either cool or warm. To conclude the series, jet launching from the interface between the magnetic rotor (the star) and the disc is studied. Synthetic profiles are calculated from numerical simulations of outflow launching by star-disc interaction. Profiles are calculated for several possible configurations of the stellar field: dipolar (with surface strengths, B_* of 1, 2 and 5 kG) or dynamo fed. Also two types of discs, passive or subjected to an $\alpha\Omega$ -dynamo, are considered. These profiles have been used to define the locus of the various models in the observational diagram: dispersion versus centroid, for the profiles of the Si III] line. Bulk motions produce an increasing broadening of the profile as the lever arm launching the jet becomes more efficient; predicted profiles are however, sensitive to the disc inclination. Models are compared with observations of the Si III] lines obtained with the *Hubble Space Telescope*.

In addition, it is shown that the non-stationary nature of star-disc winds produce a flickering of the profile during quiescence with variations in the line flux of about 10%. At outburst, accretion signatures appear in the profiles together with an enhancement of the wind, producing the correlation between accretion and outflow as reported from RU Lup, AA Tau and RW Aur observations.

Key words: stars: pre-main-sequence – stars: winds, outflows – stars: circumstellar matter – stars: formation

1 INTRODUCTION

Star formation is accompanied by heavy mass outflow. Outflows are powered by the gravitational field (through the centrifugal gear) and by the release of the magnetic energy built up in the sheared and turbulent protostellar discs. Since the very early studies of the atmospheres of the T Tauri Stars (TTSSs), it is known that during the classical T Tauri phase (~ 1 Myr old stars), TTSSs drive powerful and massive cool ($T \sim 10,000$ K) winds whose signature was first detected in the profiles of neutral and singly ionized species being the most conspicuous the optical H α line and the Mg II resonance multiplet (UV1) in the UV (Giampapa et al 1981, Penston & Lago 1983, Finkenzeller & Mundt 1984, Calvet et al 1985). The realisation that TTSSs drive cool ($T \sim 10,000$ K) jets and bipolar outflows came in the

early 80's (i.e. Schwartz 1983, Mundt et al 1987). Ever since, it is unclear which fraction of cool wind is associated with the so-called cool *stellar* wind (and which fraction is associated with the bipolar outflow). For instance, the absorption by this cool wind of the H₂ emission from the disc (produced within ~ 2 AU from the star, Herczeg et al 2004), clearly indicates that a significant fraction of the absorbing gas is associated with the large scale jet.

Though there is a general consensus on bipolar outflows being driven by the disc-star interaction and the disc wind (see i.e. Ferreira et al 2006), the nature of TTSSs *stellar* winds remains open. Hot winds are expected to be produced by the star since the strong magnetic activity and the powerful stellar corona (Preibish et al 2004) suggest that a pre-main sequence analogue to the solar coronal winds must exist. Unfortunately, this hot component has not been conclusively detected. This is caused by the complexity of the atmospheres and the disc-star interaction region in TTSSs

* E-mail: aig@mat.ucm.es

that makes difficult to disentangle the contribution from the photoionized accretion flow and the inner disc from a theoretically hypothesised hot stellar wind. In 2005, Dupr e et al, claimed to have detected, for the first time, this hot wind. These authors interpreted the absence of blueshifted emission in the O VI resonance lines in TW Hya and T Tau, as an indication of the existence of a hot wind with temperatures as high as 300,000 K and mass-loss rates of $2 \times 10^{-11} M_{\odot} \text{yr}^{-1}$ that absorbs the blue wing of the profile. As pointed out by Johns-Krull & Herczeg (2007), the lack of a blueshifted component could just be an indication of the line being formed in the accretion flow. Matter infall onto the stellar surface is channelled by the magnetic field driving to the formation of shocks at the impact points where the kinetic energy of the infalling gas is finally released. The temperature reached at the shocks can be as high as some 10^6K and the photoionizing X-ray radiation preionizes the infalling gas column that radiates over a wide range of temperatures and tracers (Lamzin 1998).

An independent line of research, the one addressed in this series, was to investigate whether the base of the jet could be hot enough to radiate at temperatures as high as 50,000 K-80,000 K, well below the temperature range of the hot stellar wind but above the fiducial temperatures of optical jets: 10,000 K-20,000 K. The motivation for this research came from the discovery of C III] and Si III] semiforbidden emission in the UV spectrum of RY Tau and RU Lup at the same velocity of the optical jet; this emission traces gas at $\log T_e \sim 4.6 - 4.8$ (G omez de Castro & Verdugo 2001). Centrifugally driven flows from magnetised accretion discs are submitted to pinching stresses $\vec{j} \times \vec{B}$ because the toroidal magnetic field (\vec{B}) collimates the current of gas along the disc axis (\vec{j}). Recollimation can drive to the formation of focal surfaces or shocks on the jet axis that are able to heat the gas to the some 10,000 K traced by the optical forbidden lines of S II] (G omez de Castro & Pudritz 1993). However, temperatures as high as 80,000 K cannot be produced in cool disc winds. In the first article of this series, we examined whether the photoionisation of cool disc winds by the stellar corona could cause the observed emission (Ferro-Font an & G omez de Castro 2003, hereafter Paper I). We found that the propagation of the stellar radiation generates a cocoon of photoionized gas around the star. The extent of the photoionized region is small (tenths of au) in dense outflows and close to the disc plane; however, it may cover the whole wind extent in diffuse winds, e.g. disc winds generated by small accretion rates ($\leq 10^{-9} M_{\odot} \text{yr}^{-1}$). Photoionisation also modifies the electron density in the plasma. The interplay between ambipolar diffusion and the radiation field controls the electron temperature of the wind that is kept around 10,000 K, well below the temperatures traced by the UV semiforbidden lines.

Disc winds are a fundamental mechanism for angular momentum transport in protostellar discs, contributing to the regulation of the accretion rate onto the star. However, most of the transport occurs in the disc itself through the magnetorotational instability (Balbus & Hawley 1991): weak fields provide a tension force that allows two orbiting fluid elements to exchange angular momentum on larger scales than the hydrodynamical viscosity scales. The magneto rotational instability acts like a dynamo, amplifying the field which is lost due to buoyancy, leading to a magnetised corona. Flares

associated with reconnection events would naturally be produced leading to the formation of a hot disc corona. Warmer disc winds, centrifugally launched from the disc corona, were shown to be able to reproduce the observed line fluxes and line ratios provided that the winds are clumpy (with filling factors about 1%) in G omez de Castro & Ferro-Font an 2005 (hereafter Paper II), the second article of this series. Warm disc winds have also been shown to be able to reproduce larger scale jet observations (see i.e. Vlahakis & Tsinganos 1999, Ferreira 2004). Warm disc winds provide an elegant and simple solution to the high jet temperatures observed in the UV however, they are not adequate to reproduce in full detail the observed physics of the line formation region. Long tails of bluewards shifted emission are detected in the Si III] and C III] plasma tracers, suggesting that the outflow launching mechanism is more efficient and, at the same time, the outflow is less collimated than predicted by the simple self-similar warm disc wind theory. As shown in Paper II, the self-similar solutions that are able to reproduce the observed jet properties (velocity and mass flow) require that the ratio between the sound speed and the escape velocity is 0.43 at the Alfv en radius. As a result, the radial expansion of the outflow - the main source of line broadening - is shifted to distances of about 10 AU from the star, where plasma cannot contribute to the Si III] and C III] emission because the densities and temperatures are very low and radiative cooling is dominated by singly ionized species (see Fig. 3 in G omez de Castro & Verdugo 2007, hereafter GdCV07). Thus, self-similar models produce winds too collimated at the base to reproduce the observed broadening of the Si III] and C III] profiles.

The high densities revealed by the Si III], C III] and C IV] line ratios indicate that this line radiation is produced very close to the star. Henceforth the radiating plasma must be strongly affected by the disc-star interaction. In fact, there is evidence that Si III] and C III] radiation can be produced in structures very close to the star such as the ionized plasma torus around RW Aur (G omez de Castro & Verdugo 2003) or the accreting shell in RY Tau (GdCV07). The physics of the interaction between the stellar magnetic field and the accretion disc is very rich, and it has been shown extensively that jet launching can be produced from this interaction region with physical temperatures and densities similar to those of stellar chromospheres (Goodson et al. 1997, von Rekowski & Brandenburg 2004, 2006). Jet launching from the interface between the magnetic rotor (the star) and the disc is much more efficient than a pure disc wind, firstly because the centrifugal gear is higher closer to the star and secondly because of the heavy mass load onto the field lines at this point. Thus, to conclude this series, we have computed the radiative output from numerical simulations of outflow launching from star-disc interaction. It will be shown that the radial flow expansion, i.e. the outflow from the disc-star interaction region, is able to reproduce the observed broadenings for magnetospheric fields of about 1-2 kG. In Section 2, the characteristics of the simulations from von Rekowski & Brandenburg (2004, 2006, hereafter vRB04 and vRB06, respectively), that are used in this work, are summarised. In Section 3, the procedure to derive line fluxes and profiles from the simulations is described. The analysis of the output profiles is developed in Section 4. A discussion

on the implications and relevance of the results is deferred to Section 5, as well as the main conclusions.

2 THE T TAURI STAR-DISC SYSTEM

2.1 The magnetospheric star-disc model

The interaction between the star and the Inner disc Boundary Layer¹ generates a sheared region fed by turbulent, magnetised material from the accretion disc. Shear amplifies the stellar magnetic field, producing a strong toroidal magnetic field component. This toroidal field and the associated magnetic pressure push the stellar poloidal field away from the stellar/disc rotation axis, inflating and opening the poloidal field lines in a *butterfly like pattern* thus producing a current layer between the stellar and the disc dominated regions as displayed in Fig. 1. The magnetic link between the star and the disc is broken and re-established periodically by magnetic reconnection. The opening angle of the current layer, as well as its extent, depends on the stellar and disc fields, the accretion rate and the ratio between the inner disc radius and the stellar rotation frequency.

In the magnetospheric models of vRB04, a slow, hot and dense outflow driven mostly by poloidal magnetic pressure is emanating from stellar regions close to the rotation axis while fast, cooler and less dense magneto-centrifugally accelerated outflows are emanating from lower stellar latitudes and from the inner disc. The main difference with the magnetospheric models of Goodson et al. (1997) is that in the Goodson models the axial (stellar) jet is fast and well-collimated - and driven by magneto-centrifugal processes (see also Hirose et al. 1997) - and the inner disc wind is divergent, whereas in vRB04 the stellar wind is slow but on the other hand some collimation is clearly seen in the inner (magneto-centrifugally accelerated) disc wind. However, the stellar wind seen in Romanova et al. (2002) is also slow, travelling into a rarefied corona. A very fast (warm and dense) stellar wind is seen in stellar dynamo models of vRB06; this wind is mostly driven by toroidal and poloidal magnetic pressure, as well as gas pressure.

2.2 Basic characteristics of the numerical models

Though a full description of the numerical simulations can be found in vRB04 and vRB06, we should briefly summarise their main properties. In both papers, the evolution of the flow, magnetic field, density and temperature is found by solving the continuity, the Navier–Stokes and the mean-field induction MHD equations for an axisymmetric system in cylindrical polar coordinates, assuming a piecewise polytropic model. Dynamo action in the disc (if present) is prescribed by a standard $\alpha^2\Omega$ dynamo (e.g. Krause & Ruedler 1980), where α is the mean-field α -effect and Ω is the angular velocity of the orbiting gas. α -quenching is included so that the disc dynamo saturates at a level close to equipartition between magnetic and thermal energies. The code uses

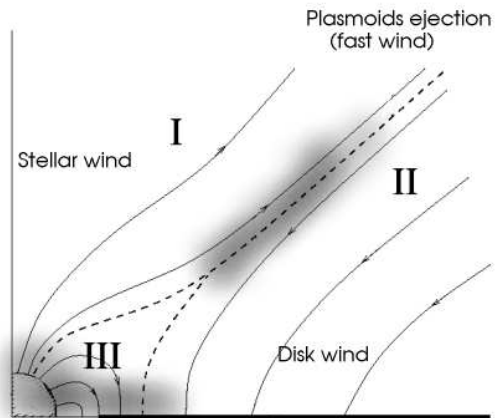


Figure 1. The interaction between the stellar magnetic field and the disc twists the stellar field lines due to the differential rotation. The toroidal magnetic field generated out of the poloidal flux and the associated magnetic pressure tends to push the poloidal field lines outwards, inflating them, and eventually braking the magnetic link between the star and the disc (boundary between regions I and II). Three basic regions can be defined: Region I dominated by the stellar wind, Region II dominated by the disc wind and Region III dominated by stellar magnetospheric phenomena. The dashed lines trace the boundaries between these three regions. The continuous lines indicate the topology of the magnetic field and the shadowed areas represent regions where magnetic reconnection events are likely to occur, producing high energy radiation and particles (from Gómez de Castro 2004).

dimensionless variables that have been scaled using as reference values a typical sound speed of the coronal gas (100 km s^{-1}) and a typical surface density at the surface of the disc (1 g cm^{-2}). Furthermore, the mass of the star has been taken as $1 M_{\odot}$ (solar mass), the mean specific weight as $\mu = 0.6$ and the polytropic index as $\gamma = 5/3$. The computations have been carried out in a domain of extent 0.2 AU in the radial (ϖ) direction and $\pm 0.1 \text{ AU}$ above/below the disc mid-plane; mesh sizes are $\delta\varpi = \delta z = 0.001 \text{ AU}$. The inner edge of the disc is at 4 stellar radii (in the models with stellar dipolar magnetosphere; cf. Table 1) or at 2.4 stellar radii (in the model with stellar dynamo), which in both cases corresponds to 12 solar radii. The disc extends to the outer boundary of the computational domain.

The vRB04 models represent a step forward over the self-similar warm disc winds models of Paper II. Around the inner edge of the disc, the interaction with the stellar magnetosphere and the stellar wind is taken into account. Also, the rigidity of the self-similarity constraint is lost. Furthermore, the Lorentz force $\vec{j} \times \vec{B}$ is included in the Navier–Stokes equation, as well as the generation of magnetic fields by the standard $\alpha^2\Omega$ dynamo in the disc. The saturation level of the disc dynamo is governed by the equipartition between magnetic and thermal energies in the disc. In accordance with observations of protostellar star-disc systems, the model implements a dense, cool disc embedded in a rarefied, hot disc corona. This is achieved by prescribing an entropy contrast between the disc and corona so that specific

¹ The shearing layer between the region dominated by the stellar magnetic field and the gravitationally dominated Keplerian disc has a finite extent.

entropy is smaller within the disc and larger in the corona, and by choosing hydrostatic equilibrium as the initial state. Therefore, detailed modelling of the coronal heating physics is avoided by prescribing a "thermal" frontier between disc and corona that is based on the observational properties of accretion discs (piecewise adiabatic model in disc, corona and star). However, temperature is evolving with time, in particular in the disc corona as one can clearly see in the relevant figures. Assuming a perfect gas, the continuity equation is re-formulated as an evolution equation for specific enthalpy, which is directly related to temperature. The specific enthalpy is then combined with the gravitational potential to form the potential enthalpy.

In a sense, the disc in the vRB04 simulations can be understood as a dynamical boundary that regulates the extra electromotive force caused by the disc dynamo and taps the mass flow into the wind and onto the accreting star. vRB04 adds to the dynamics of the self-similar models in Papers I & II but shares a similar thermal treatment allowing a straightforward comparison.

The full set of simulations in vRB04 and vRB06 explores the role of disc-star interaction in mass ejection for various configurations of the stellar field (a dipolar magnetosphere or a mean-field $\alpha^2\Omega$ dynamo generated field) and strengths (models with different stellar surface fields are analysed). The simulations also explore the role of magnetically active discs (with $\alpha^2\Omega$ dynamos) in the dynamical evolution of the system by comparing the active disc evolution with that of passive discs. In all the simulations, the three basic winds: hot stellar wind, warm disc wind and episodic ejections from reconnection in the star-disc current layer are readily identified. In this work the radiative output has been calculated only for a subset of these simulations.

Firstly, we have selected a reference model to analyse whether and how the temporal evolution of the simulated star-disc system shows in the profiles of the spectral tracers of the outflows. This is model "M1" in vRB04. The stellar magnetosphere is initially a dipole threading the disc but with time can freely evolve outside the anchoring region away from the stellar surface; the dipole is aligned with the disc axis and has a strength at the stellar surface of $B_* \sim 1\text{kG}$. The disc is assumed to be undergoing a significant dynamo action with $\alpha_0 = -0.1$. This is the so-called "Reference" model in Table 1. The thermal properties of the disc wind at the launching points in the corona are similar to those derived in Paper II for warm disc winds, i.e.:

$$T = 6.4865 \times 10^4 \text{K} y^{0.05} \langle \mu \rangle \left(\frac{M_*}{M_\odot} \right) \left(\frac{\varpi_0}{0.1\text{AU}} \right)^{-1} \quad (1)$$

where M_* is the mass of the T Tauri star, ϖ_0 is the radial distance of the wind foot point (in the disc corona) and y is the ratio between the outflow density at ϖ_0 and at the Alfvén radius (see Paper II for more details). The temperature drops as ϖ^{-1} at the base of the disc wind, similarly to what derived in vRB04 for the *Reference* model (see i.e. Fig. 2 in vRB04). Notice that in Paper II these conditions are set to reproduce the observed large scale properties of protostellar jets following Vlahakis & Tsinganos (1999). In vRB04, the thermal properties of the wind are derived from the specific enthalpy, h , that is included in the modified Navier-Stokes and continuity equations (von Rekowski et al. 2003). The system is piecewise adiabatic and the equa-

Table 1. Summary of the simulations analysed

Iden	Stellar field	disc field
<i>Reference</i>	Dipolar, $B_* \sim 1\text{kG}$	$\alpha^2\Omega$ dynamo with $\alpha_0 = -0.1$
<i>Mag-2kG</i>	Dipolar, $B_* \sim 2\text{kG}$	$\alpha^2\Omega$ dynamo with $\alpha_0 = -0.1$
<i>Mag-5kG</i>	Dipolar, $B_* \sim 5\text{kG}$	$\alpha^2\Omega$ dynamo with $\alpha_0 = -0.1$
<i>Passive</i>	Dipolar, $B_* \sim 1\text{kG}$	No dynamo
<i>Dynamo*</i>	$\alpha^2\Omega$ dynamo, $\alpha_0 = 1.5$	$\alpha^2\Omega$ dynamo with $\alpha_0 = -0.15$

tion of state a polytrope, thus the sound speed is given as $c_s^2 = (\gamma - 1)h$, with $\gamma = 5/3$, and the temperature is derived directly from $h = c_p T$.

In addition, we have selected a set of models to study the variation of the quiescent profiles with the strength of the magnetospheric field. Models with $B_* \sim 2\text{kG}$ and $B_* \sim 5\text{kG}$ have been analysed. These models are quoted as "Mag-2kG" and "Mag-5kG", respectively. As in the reference model, the disc is assumed to be undergoing dynamo action with $\alpha_0 = -0.1$.

The next step has been to explore whether the presence of an active or passive disc can be detected in the profiles. For this purpose we have analysed a simulation similar to that of the "Reference" model but with a passive disc (no disc dynamo); this model is quoted as "Passive" in Table 1.

Finally, we have analysed how the profiles change with the characteristics of the stellar field, i.e. we have investigated whether introducing an active dynamo in the star modifies the line profiles. This model is quoted as "Dynamo*"; the star is considered to be fully convective with the stellar dynamo rooted up to about 5 solar radii and $\alpha_0 = +1.5$ for the stellar dynamo.

A summary with the names and main magnetic properties of the models is given in Table 1.

The vRB04 models analyse the dynamical evolution of the star-disc interaction during total run times between ~ 150 d and ~ 1900 days. However, the time scale analysed in this work is significantly shorter: about 75 d in the "Reference" model where the effect of outburst compared to quiescence is studied in the profiles. This shorter time scale is, in general, about twice the typical matter crossing time from the outer to the inner disc border: $(\varpi_{\text{out}} - \varpi_{\text{in}})/u_{\varpi} \approx (0.2 - 0.06)\text{AU}/7\text{kms}^{-1} \sim 34.5$ d. In vRB04, matter is injected locally wherever and whenever it is needed in the disc region, in order to model mass accretion from the outer parts of the disc to the inner parts. This might produce artificially high mass loss rates in the long term, especially around the inner disc edge where mass outflow is more efficient (see vRB04 for a detailed discussion on the implications of this approach). Selecting periods shorter than the crossing time minimises the effect of matter injection.

3 COMPUTATION OF THE LINE PROFILES

Flow kinematics is handy described by three components:

- Motion along the rotation (or z) axis (vertical flow component): V_z
- Rotation given by the toroidal flow component: V_t

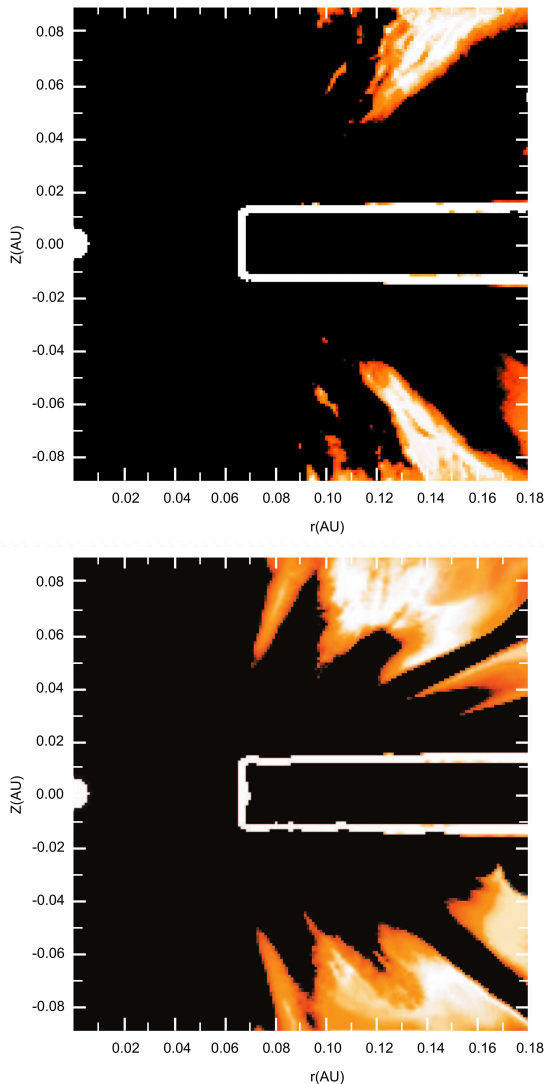


Figure 2. Si III] emissivity maps of the reference model during quiescence (top) and in outburst (bottom). Notice that at outburst the Si III] emitting region is large and reaches closer to the star.

- Expansion away from the rotation axis (radial flow component): V_{ϖ}

The numerical simulations provide as output the density ρ_k , temperature T_k , the three velocity components ($V_{z,k}$, $V_{t,k}$, $V_{\varpi,k}$) and the three magnetic field components at any given cell, k , of the computational mesh. As the models are axisymmetric, the simulations provide the same temperature and density for a cylindrical ring around the disc axis. As the C III]₁₉₀₈ and the Si III]₁₈₉₂ lines are semiforbidden, the output radiation can be directly computed from the emissivity and the volume of the ring. The spectral distribution of the radiation is then computed for a given k -ring using the projection of the ring velocity into the line of sight. At

any point in the ring, the velocity projected into the line of sight² is given by

$$V_{\text{rad},\alpha} = -V_{\varpi,k} \cos \alpha \sin i - V_{z,k} \cos i + V_{t,k} \sin \alpha \sin i, \quad (2)$$

where i is the inclination of the star (the angle between the line of sight and the disc axis) and α is the angle between the stellar meridian that contains the line of sight and the meridian where the gas parcel under consideration in the k -ring is located; each ring has been subdivided into 100 cells with $\Delta\alpha = 2\pi/100$ for the calculation of the profile. The temperature T_k is taken into account to compute the effect of thermal broadening.

The emissivity of any k -ring is calculated for the semiforbidden line of Si III]. C III] emissivity was also calculated but the density is high and the line is collisionally quenched in most of the simulated area thus it was not further studied. The atomic parameters for the lines were taken from the Chianti Atomic Data Base³ (see Appendix A). Collisional rates have been calculated using thermally averaged collision strengths making use of Burgess & Tully (1992) fits and rules. For each T_k , the ionisation fraction has been calculated and the electron density, n_e , has been derived. The electron temperature, T_e , is assumed to be equal to T_k in each given k -ring.

Si III] emissivity, j , corresponding to the transition between levels j and m is given by

$$j = \frac{n_j A_{j,m} h \nu_{j,m}}{f(n_e, T_e) \frac{n_j}{n_{\text{Si III}}} \frac{n_{\text{Si III}}}{n_{\text{Si}}} \frac{n_{\text{Si}}}{n_{\text{H}}} \frac{n_{\text{H}}}{n} n A_{j,m} h \nu_{j,m}}. \quad (3)$$

The population of the relevant levels ($n_j/n_{\text{Si III}}$) has been computed directly with the Chianti code for each temperature and electron density. The ionisation fractions ($n_{\text{Si III}}/n_{\text{Si}}$) have been calculated assuming ionisation equilibrium. Solar abundances are used for $n_{\text{Si}}/n_{\text{H}}$ and the ionisation fractions to determine n_{H}/n . $f(n_e, T_e)$ is a correction factor that takes into account the collisional quenching of the line⁴.

For a given inclination, the theoretical Si III] profiles are computed from the simulation data by adding the contributions from all the k -rings with $\varpi \geq 4R_*$; this condition was partly set to avoid confusion with any stellar-associated component. In addition, the numerical simulations analysed (vRB04, vRB06) are not adequate to follow the thermal instabilities in the boundary layer between the star and the disc and, as a consequence, the physical conditions and the derived radiative output are not reliable for this region of the computational mesh.

For each simulation in Table 1, the Si III] profile has been computed for each time unit (approximately 3 days) to track the profile variability, to separate quiescence from

² The minus sign has been set to indicate the velocity shift as seen by the observer, so negative velocities (or “blueshifts”) are associated with gas motions towards the observer.

³ URL: www.damtp.cam.ac.uk/user/astro/chianti/

⁴

$$f(n_e, T_e) = \frac{A_{j,m}}{A_{j,m} + n_e q_{j,m}},$$

where $n_e q_{j,m}$ and $A_{j,m}$ are the rates for downward collisional and radiative transitions, respectively. Note that when the line is collisionally quenched, then $f(n_e, T_e) \propto n_e^{-1} T_e^{1/2} < \Upsilon > (T_e)$.

outburst and to compute the line flickering during the quiescence phase.

4 ANALYSIS OF THE OUTPUT PROFILES

A given profile is a set of pairs (V_{rad}, f) where f is the total flux radiated by the outflow into the line of sight with projected radial velocity in the range $[V_{rad}-5 \text{ km s}^{-1}, V_{rad}+5 \text{ km s}^{-1}]$. V_{rad} ranges from -300 km s^{-1} to 300 km s^{-1} , taken in steps of 10 km s^{-1} that oversample the thermal broadening (typically $\sim 30 \text{ km s}^{-1}$) by a factor of 3.

The system alternates episodic ejections of matter (outbursts) with quiescent periods where accretion is dominant (see vRB04). During outburst, the magnetic star-disc link is basically broken: the stellar dipolar field lines connecting to the disc are opening up and matter is flowing along the open stellar and disc field lines forming an outer stellar wind and enhanced inner disc wind. In Fig. 2, Si III] emissivity maps are shown of the reference model at four different times: the first three images are during the quiescence period while the last one is during outburst.

A reliable comparison between the theoretical profiles and the observed profiles requires the identification of a set of statistically meaningful quantities to describe the profiles. We have used for this purpose:

- The *velocity of the peak of the line*, V_p .
- The *line asymmetry*, A , defined as: $A = \frac{\sum_{v_b}^0 f}{\sum_{v_r} f}$, where f represents the flux at projected radial velocity v , v_b marks the minimum radial velocity of the blue wing of the line, and v_r marks the maximum radial velocity of the redwing of the line.
- The *line centroid*, $\langle V \rangle$, defined as: $\langle V \rangle = \frac{\sum_{v_b}^{v_r} f * v}{\sum_{v_b}^{v_r} f}$.
- The *dispersion*, σ , defined as: $\sigma = \frac{\sum_{v_b}^{v_r} f * (v^2 - \langle V \rangle^2)}{\sum_{v_b}^{v_r} f}$.

Moreover, as the redwing of the profile may have a variable contribution from mass infall (see RY Tau profiles in GdCV07), dispersion and line centroid have also been evaluated only for the blue wing of the profile:

- The *line centroid of the blueshifted emission*, $\langle V_b \rangle$, defined as: $\langle V_b \rangle = \frac{\sum_{v_b}^0 f * v}{\sum_{v_b}^0 f}$.
- The *dispersion in the blueshifted emission*, σ_b , defined as: $\sigma_b = \frac{\sum_{v_b}^0 f * (v^2 - \langle V_b \rangle^2)}{\sum_{v_b}^0 f}$.

In Fig. 3 the temporal variations of these quantities are plotted for a whole quiescence-outburst cycle for the "Reference" model. The quiescence period can be readily identified, as well as the outburst period when the profiles are more weighted to the blue and broader than in quiescence. In other words, the quantities more sensitive to trace mass ejection are: σ , σ_b and $\langle V_b \rangle$ which, in turn, are rather insensitive to the inclination of the source with respect to the line of sight.

The effects in the Si III] profiles due to an outburst are shown in Fig. 4 for the reference model: the line broadens and the emission region expands towards the boundaries of the computational domain. However, during outburst there is also some contribution from matter infall (accretion) to the profile (see bottom panels in Fig. 4), when some matter

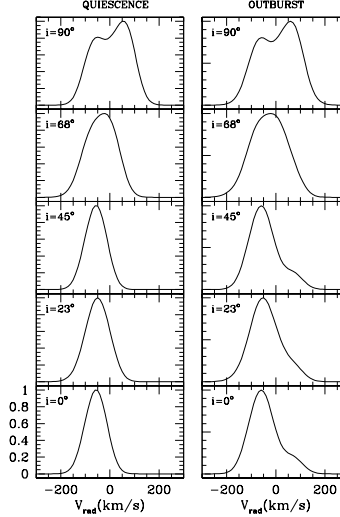


Figure 4. Theoretical profiles of the Si III] line derived from the reference model of the numerical simulations. The time averaged profile in quiescence is plotted in the left hand panels and the time averaged profile in outburst is plotted in the right hand panels, for various inclinations.

is channelled along the rising and closing field lines into an infalling accretion flow - at the same time as enhanced winds are starting or ceasing to form. In summary, a clear correlation between outflow and accretion signatures is predicted from these numerical simulations.

Though these results are extremely promising because the correlation between infall and outflow signatures has been reported for various cTTSs (i.e. RU Lup by Stempels & Piskunov 2002, RW Aur by Gómez de Castro & Verdugo 2003 and AA Tau by Bouvier et al 2007), they should be considered just as a first order approach; the axisymmetry assumption imposed in the code and in the calculation of the radiative output, forces one to assume that large plasma tori are ejected (accreted) along the disc axis at the time of outburst (as the smoke rings produced by master smokers). However, in the T Tauri systems mass ejection occurs in the form of blobs (plasmoids) from reconnecting magnetic fields, which have a much smaller emitting volume than the tori assumed in this axisymmetric computation. As a consequence the fluxes predicted in this paper for outburst (both infall and outflow) are overestimated. For this reason, we should concentrate on the analysis of the profiles during the quiescence phase.

During quiescence, flickering produces variations of σ_b and $\langle V_b \rangle$ that are highly correlated, as shown in Fig. 5 for two numerical simulations (*Reference* and *Dynamo**) and two possible inclinations; the correlation coefficient is between 0.96 and 0.9998 depending upon the simulation. This high correlation indicates that the shape of the line profile does not vary significantly - to the first moment - during quiescence, and, in turn, the variations in the profile caused by mass ejections are averaged out by the large broadening induced by the thermal motions of the gas. The largest

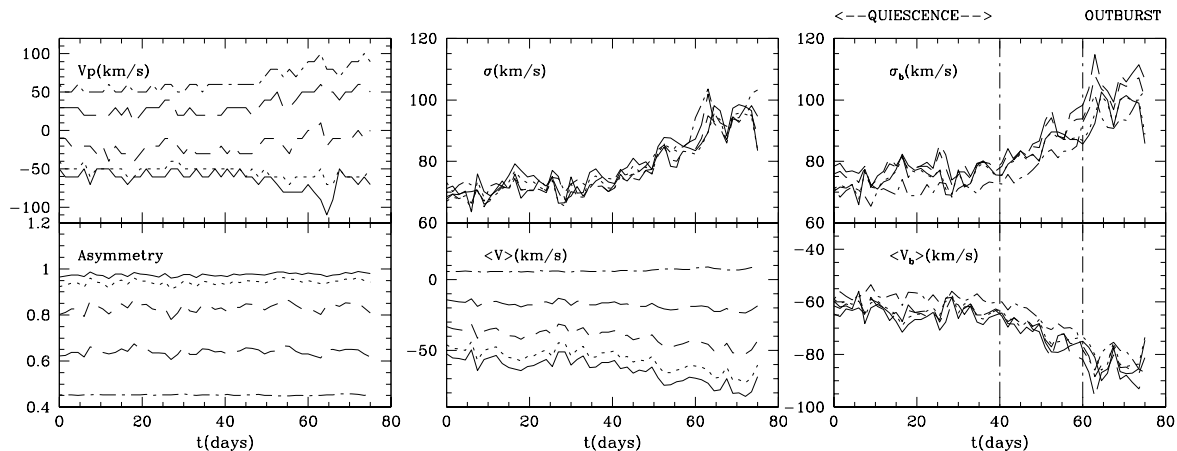


Figure 3. Temporal variations of the statistical quantities used to characterise the line profiles in the simulation of the (magnetospheric) reference model. The data corresponding to inclinations of 0° , 23° , 45° , 68° and 90° are represented by solid, dotted, short-dashed, long-dashed and dot-dashed lines, respectively. The time refers to after the start of the analysed time series.

variations in σ_b are observed for the pole-on (inclination 0°) orientation.

The time-average values $\bar{\sigma}_b$ and $\langle \tilde{V}_b \rangle$ are given for each simulation and five inclinations during the quiescence period in Table 2. The dispersion about these average values is also given; note that this dispersion reflects the short-time scale variability (the flickering) of the highly non-stationary star-disc interaction. The theoretical line flux calculated from the simulations is provided in the last column. As no extinction effects are taken into account in the calculation of the line profiles and fluxes, the fluxes given in the table are the same for all the orientations in each model⁵. The flickering during quiescence produces slight variations in the line fluxes in the range of $\sim 10\%$. The fluxes derived are similar to those derived for warm disc models (see Table 2 in Paper II). Average profiles for the various models and three inclinations are displayed in Fig. 6.

Several general conclusions can be derived from the analysis of the quantities and profiles:

- Enhancing the dipolar stellar magnetic field enhances $\bar{\sigma}_b$, $\langle \tilde{V}_b \rangle$ and their respective dispersions. Thus these quantities are good tracers of the magnetic field strength and therefore of the wind launching capability. The reason is that the centrifugal gear, for a given accretion rate, depends on the location of the Alfvén surface. Stronger fields push this surface further away from the star, thereby raising the wind terminal speed as well as increasing the radius ϖ of the ring radiating in Si III], and thus increasing also the dispersion of the projected velocity in the region where the emitting gas is located.

- $\bar{\sigma}_b$ and $\langle \tilde{V}_b \rangle$ are sensitive to the viewing angle (the inclination of the line of sight with respect to the star) for strong stellar dipolar fields or for stellar fields that are dynamo induced. In general, the larger the inclination the larger the values of $\bar{\sigma}_b$ and $\langle \tilde{V}_b \rangle$; however, the maxima of $\bar{\sigma}_b$ and $\langle \tilde{V}_b \rangle$ are achieved at inclination $\sim 68^\circ$, which

Table 2. The $\bar{\sigma}_b$ and $\langle \tilde{V}_b \rangle$ quantities (averaged over time in the quiescence period) derived from the simulations

Iden	Inclination	$\langle \tilde{V}_b \rangle$	$\bar{\sigma}_b$	Flux ($\text{erg s}^{-1} \text{cm}^{-2}$)
<i>Reference</i>	0°	-64 ± 4	75 ± 4	$(4.0 \pm 0.5) \times 10^{-8}$
	23°	-63 ± 3	74 ± 3	
	45°	-63 ± 2	77 ± 3	
	68°	-64 ± 3	78 ± 3	
	90°	-58 ± 2	71 ± 2	
<i>Mag-2kG</i>	0°	-81 ± 7	93 ± 8	$(3.9 \pm 0.6) \times 10^{-8}$
	23°	-81 ± 6	96 ± 7	
	45°	-85 ± 7	104 ± 8	
	68°	-90 ± 8	107 ± 9	
	90°	-82 ± 8	97 ± 9	
<i>Mag-5kG</i>	0°	-89 ± 14	103 ± 16	$(3.9 \pm 0.6) \times 10^{-8}$
	23°	-90 ± 12	109 ± 15	
	45°	-101 ± 11	124 ± 14	
	68°	-108 ± 11	130 ± 13	
	90°	-101 ± 14	121 ± 18	
<i>Passive</i>	0°	-45 ± 6	54 ± 6	$(1.9 \pm 0.2) \times 10^{-8}$
	23°	-45 ± 6	57 ± 6	
	45°	-48 ± 6	63 ± 7	
	68°	-50 ± 6	65 ± 7	
	90°	-46 ± 4	60 ± 5	
<i>Dynamo*</i>	0°	-64 ± 8	77 ± 9	$(3.1 \pm 0.8) \times 10^{-8}$
	23°	-70 ± 5	86 ± 6	
	45°	-83 ± 7	102 ± 8	
	68°	-89 ± 10	108 ± 11	
	90°	-85 ± 10	103 ± 11	

roughly corresponds to the angle between the field lines and the disc axis in the main ejection region: the current sheet region between the disc field and the stellar field.

- Passive discs produce narrow lines. There are two reasons for that. As discussed in vRB04, the initial magnetic field in the disc due to the penetrating stellar magnetosphere is expelled out of the disc and the wind flows nearly parallel to the disc surface in the low corona. As a result, the velocity dispersion is smaller. In addition, the Alfvén surface is

⁵ The circumstellar extinction is inclination dependent since it is caused by dust lifted from the disc

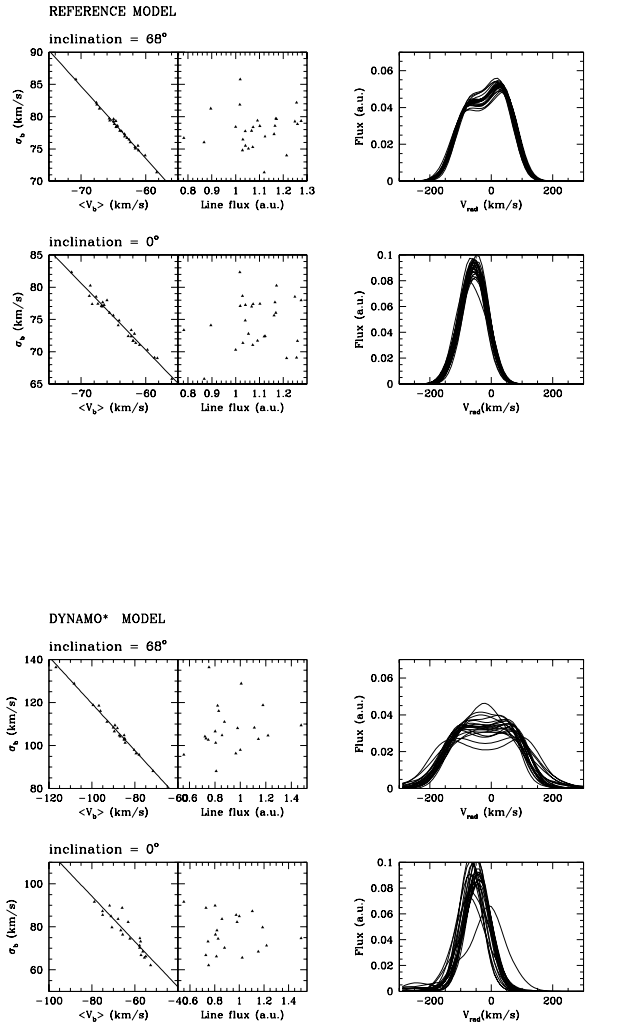


Figure 5. Left panels: variation of σ_b versus $\langle V_b \rangle$ and versus the line flux (in arbitrary units) during quiescence and inclinations 68° and 0° (in the top and bottom panels, respectively). The temporal line profile variations during quiescence are represented in the right panels. *Top*: "Reference model", *bottom*: "Dynamo*" model.

located at the innermost boundary of the star-disc system and thus the centrifugal gear is negligible.

- Active stellar dynamos are able to generate a rapid out-flow even for a moderately strong magnetic field. The reason is because in the "Dynamo*" model the stellar wind is mostly driven by both poloidal and toroidal magnetic pressure, as well as by gas pressure.

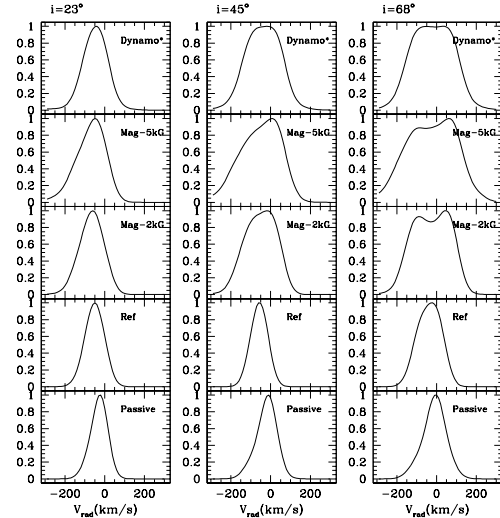


Figure 6. Theoretical profiles of the Si III] line during quiescence for the five numerical models analysed (see Table 1) and three inclinations with respect to the line of sight: 23° , 45° and 68° .

5 COMPARISON WITH OBSERVATIONS AND SUMMARY

In Fig. 7, the time-averaged values $\tilde{\sigma}_b$ and $\langle \tilde{V}_b \rangle$ are plotted for the various models studied in this work. The error bars mark the dispersion around the average values in quiescence, caused by the flickering. All the inclinations are plotted and models are colour coded. The general trends described in the previous section are clearly apparent.

$\tilde{\sigma}_b$ and $\langle \tilde{V}_b \rangle$ are also plotted for warm disc winds (purple squares) for the analytical solutions of Gómez de Castro & Ferro-Fontán (2005). As expected, warm disc wind solutions are less efficient than winds driven from the star-disc boundary layer.

There is a correlation between $\tilde{\sigma}_b$ and $\langle \tilde{V}_b \rangle$, extending from the profiles derived in the numerical simulations of this work to warm disc winds (to some extent). This correlation traces the increasing efficiency of MHD centrifugally driven winds and shows that larger terminal speeds are associated with larger bulk motions at the base. Notice that inclination effects are difficult to sort out in this diagram.

5.1 The observed Si III] profiles

The information available on the Si III] profiles of TTSS come from the observations carried out by Gómez de Castro et al (2003, hereafter GdCVFF03) with the HST. The Si III] profiles are plotted in Fig. 8, as well as the C III] lines needed for the density diagnostic. All the targets (unless AK Sco) have reported jets allowing a clear identification of the out-flow signature (see Table 3). As the size of the spectrograph slit was 0.2 arcseconds, any extended structure within 28 AU could contribute to the line flux.

The contribution from the large scale jet to the line flux can be discriminated by the density of the emitting plasma. The electron density in the jet decreases very rapidly with z :

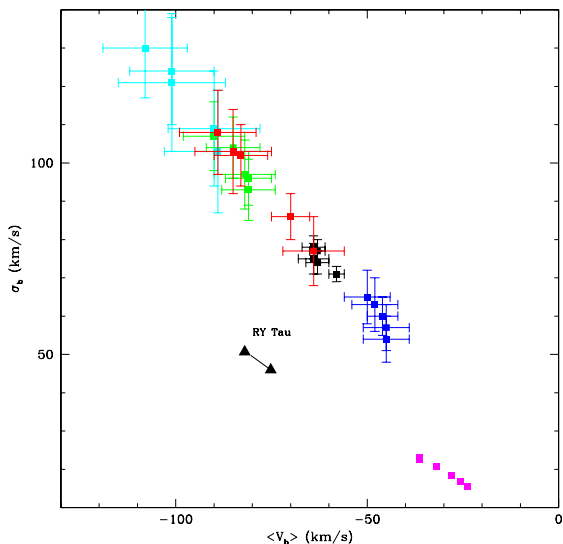


Figure 7. Representation of σ_b versus $\langle V_b \rangle$ for all models and inclinations of Table 2. The time-averaged values $\bar{\sigma}_b$ and $\langle \tilde{V}_b \rangle$ are represented as squares, while the error bars indicate true temporal variations of the profiles during quiescence. Dark blue, black, green and light blue are used to represent the models: Passive, Reference, Mag-2kG and Mag-5kG, respectively. Red is used to represent the Dynamo* model. Purple squares at the bottom right represent predictions from the warm disc wind models by Gómez de Castro & Ferro-Fontán (2005). The *observed values* for the TTS: RY Tau are plotted as two big black triangles, representing the two extreme values that can be derived from the observations carried out with the HST in 1998 (Gómez de Castro & Verdugo 2001, 2007).

from $\sim 10^9 - 10^{10} \text{ cm}^{-3}$ at the base, to $\sim 10^4 - 10^6 \text{ cm}^{-3}$ in the jet due to the rapid radial expansion of MHD centrifugally driven winds. At the low densities of the jet, the forbidden lines of [Si III]($\lambda 1983$) and [C III]($\lambda 1907$) are stronger than their semiforbidden counterparts. Also, the ratio Si-III]/CIII] is < 1 (Keenan et al 1992), as observed in the UV spectra of protostellar jets and Herbig-Haro objects (see Gómez de Castro & Robles 1999 for a compilation).

This is not observed in the HST/STIS spectra of TTSs as shown in Fig. 8 (from GdCVFF03). Typically, the Si III] and C III] lines have similar strengths. The forbidden [C III] line is only detected in T Tau and RU Lup and, only in T Tau, has a non negligible contribution to the Si III] flux. Thus Si III] emission is produced at the base of the outflow in most of the sources.

The Si III] flux may include additional contributions from accretion shocks and the stellar magnetosphere/atmosphere. Discriminating between these three components is much more difficult since they share similar temperature and density regimes.

RY Tau is the only TTS that has been observed twice in the Si III] lines allowing to separate cleanly the contribution from accretion and outflow becoming an ideal test for the models. $\bar{\sigma}_b$ and $\langle \tilde{V}_b \rangle$ for RY Tau (from GdCV07) are also plotted in Fig. 7. Notice that the line centroid is too blueshifted for the observed dispersion. This is because the contribution from the outflow is dominated by a narrow

Table 3. Properties^a of the TTSs observed in Si III]

Iden	Jet velocity (km/s)	$V \sin i$ (km/s)	i ($^\circ$)
DE Tau	-125 ⁽¹⁾	10 ⁽⁴⁾	-
T Tau	-111 ⁽²⁾	20.1 ⁽⁴⁾	20 ⁽⁶⁾
RW Aur	-167 ⁽²⁾	17.2 ⁽⁴⁾	40 ⁽⁶⁾
RU Lup	$< -170 >$ ⁽³⁾	-	24 ⁽⁷⁾
AK Sco	-	19 ⁽⁵⁾	63 ⁽⁵⁾
RY Tau	-80 ⁽²⁾	52.2 ⁽⁴⁾	86 ⁽⁸⁾

References: (1) Hartigan et al 1995; (2) Hirth et al 1997; (3) Takami et al 2001; (4) Clark & Bouvier 2000; (5) Andersen et al 1989; (6) Ardila et al 2002; (7) Stempels et al 2007; (8) Muzzerolle et al 2003.

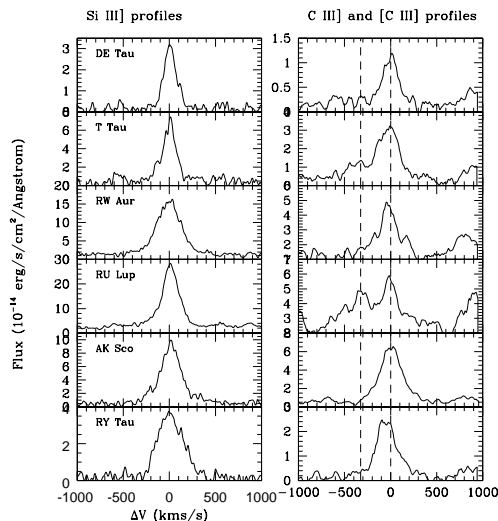


Figure 8. Measured Si III], C III] and [C III] profiles of TTSs (from GdCVFF03). The rest velocity corresponds to the rest wavelength of the Si III] and C III] lines in the left and right panels, respectively. The "velocities" of the [C III] and C III] lines are marked with dashed lines in the right panel for clarity.

blueshifted component with a long tail to redwards shifted velocities (see Fig 1 in GdCV07). This disagreement between theory and observations can be caused by the lack of cylindrical symmetry of the outflow (i.e. mass ejected as blobs from the current layer).

5.2 The $\bar{\sigma}$ versus $\langle \tilde{V} \rangle$

The $\bar{\sigma}$ versus $\langle \tilde{V} \rangle$ diagram is better suited to break the inclination degeneracy and examine the relevance of outflows with respect to magnetospheric processes in TTSs. The centroid of the line emission from the wind moves to higher blueshifts as the inclination with respect to the line of sight decreases however, no significant inclination effects are expected from magnetospheric models.

The values of $\bar{\sigma}$ and $\langle \tilde{V} \rangle$ derived from the Si III] profiles (see Fig. 8) are plotted for comparison. Notice that $\langle \tilde{V} \rangle \simeq 0$ for most sources and that there is not any trend

related with the inclination. This suggests that that Si III] emission is dominated by circumstellar structures rather than by disc winds. In fact, RW Aur, the star with the highest dispersion, is surrounded by a torus/belt of ionized plasma (Gómez de Castro & Verdugo, 2003). However, even stars that have not this kind of circumstellar structures, as DE Tau, display profiles with large broadenings that cannot be accounted solely by stellar rotation. Thus, it seems that the dominant contribution to the Si III] emission is produced in extended magnetospheric structures where the large broadening traces either the accretion flow (Hartmann 2009) or with large macro-turbulence fields, as the hypothesised to reproduce the broad profiles of AK Sco (Gómez de Castro 2009).

A small contribution from the outflow to the Si III] flux is detected RU Lup, T Tau and RY Tau (once the contribution from accretion is subtracted). It shows as a blueshifted shift of the line centroid. Unfortunately, further observations are required to disentangle magnetospheric and wind contributions prior to an accurate diagnostic of the wind drives.

We would like to conclude this work with a word of caution. This research is limited by the characteristics of the simulations analysed, such as the axisymmetry, the rather small extent of the computational domain and the very efficient tapping of thermal energy imposed by the polytropic approach in the simulations. More realistic models implementing radiative cooling and adaptive mesh refinement techniques to track the thermal instabilities are currently under development. These new simulations will produce more detailed models of the dynamics and the radiative output from the disc-star interface; however, they will not modify the strong dependence of the profiles on the inclination shown in Fig. 8, which is caused by the coupling between ejection and rotation and holds even on scales of 0.1 AU.

ACKNOWLEDGMENTS

Ana I. Gómez de Castro acknowledges the support from the Ministries of Science and Education (MEC) and Science and Innovation (MiCIn) of Spain for support through research grants AYA2007-67726, AYA2008-06423 as well as the regional government of Madrid for support through grant S-505/ESP/0237.

REFERENCES

- Andersen, J., Lindgren, H., Hazen, M.L., Mayor, M., 1989, *A&A*, 219, 142
 Ardila, D.R., Basri, G., Walter, F.M. et al., 2002, *ApJ*, 566, 1100
 Bouvier, J., Alencar, S. H. P., Bouvier, T., Dougados, C., Balog, Z., Grankin, K., Hodgkin, S. T., Ibrahimov, M. A., Kun, M., Magakian, T. Yu., Pinte, C., 2007, *A&A*, 463, 1017
 Burgess, A., Tully, A., 1992, *A&A*, 254, 436
 Calvet, N., Basri, G., Imhoff, C.L., Giampapa, M.S., 1985, *ApJ*, 293, 542
 Clarke, C.J., Bouvier, J., 2000, *MNRAS*, 319, 457
 Ferreira, J., Dougados, C., Cabrit, S., 2006, *A&A*, 453, 785

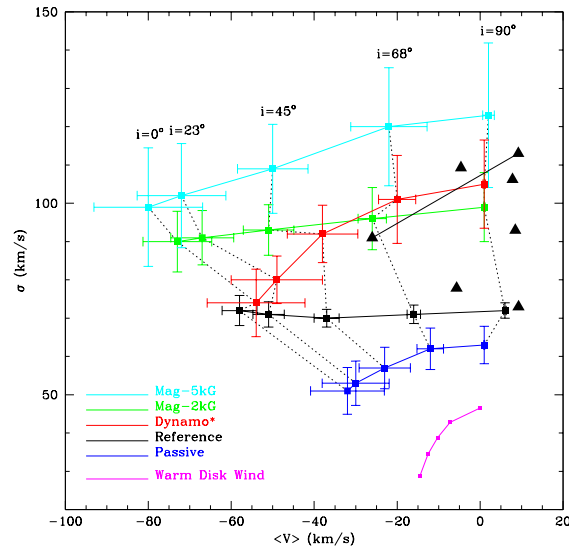


Figure 9. Representation of σ versus $\langle V \rangle$ for all models and inclinations of Table 2. The time-averaged values $\bar{\sigma}$ and $\langle \bar{V} \rangle$ are represented as squares, while the error bars indicate true temporal variations of the profiles during quiescence. Dark blue, black, green and light blue are used to represent the models: Passive, Reference, Mag-2kG and Mag-5kG, respectively. Red is used to represent the Dynamo* model. Purple squares at the bottom right represent predictions from the warm disc wind models by Gómez de Castro & Ferro-Fontán (2005). The observed values for all the TTSs observed with the HST/STIS (DE Tau, AK Sco, RY Tau, RW Aur, T Tau and RU Lup) are plotted as big black triangles. The two observations of RY Tau are plotted; the less blueshifted include the contribution from the accretion flow as in the observing campaign in 2001.

- Ferro-Fontán, C., Gómez de Castro, A.I., 2003, (Paper I)
 Finkenzeller, U. Mundt, R., 1984, *A&AS*, 55, 109
 Giampapa, M.S., Calvet, N., Imhoff, C.L., Kuhl, L.V., 1981, *ApJ*, 251, 113
 Gómez de Castro, A.I., Pudritz, R. E., 1993, *ApJ*, 409, 748
 Gómez de Castro, A.I., Robles, A., 1999, INES Access Guide No. 1, Herbig-Haro Objects. ESA SP-1237.
 Gómez de Castro, A.I., Ferro-Fontán, C., 2005, (Paper II)
 Gómez de Castro, A.I., Verdugo, E., 2001, *ApJ*, 548, 976
 Gómez de Castro, A.I., Verdugo, E., 2003, *ApJ*, 597, 443
 Gómez de Castro, A.I., Verdugo, E., Ferro-Fontán, C., 2003, *The Future of Cool-Star Astrophysics: 12th Cambridge Workshop on Cool Stars, Stellar Systems, and the Sun*, eds A. Brown, G.M. Harper, and T.R. Ayres, University of Colorado, p. 40-49
 Gómez de Castro, A.I., Verdugo, E., 2007, *ApJ*, 654, L91
 Gómez de Castro, A.I., 2009, *ApSS*, 320, 97
 Goodson, A.P., Winglee, R.M., Böhm, K.-H., 1997, *ApJ*, 489, 199
 Hartigan, P., Edwards, S., Ghandour, L., 1996, *ApJ*, 452, 736
 Hirth, G.A., Mundt, R., Solf, J., 1997, *A&AS*, 126, 437
 Hirose, S., Uchida, Y., Shibata, K., Matsumoto, R., 1997, *PASJ*, 49, 193
 Keenan, F.P., Feibelman, W.A., Berrington, K.A., 1992, *ApJ*, 389, 443

- Krause, F., Rüdler, K.-H., 1980, Mean-Field Magnetohydrodynamics and Dynamo Theory, Akademie-Verlag, Berlin
- Johns-Krull, C.M., Valenti, G.J., 2007, *ApJ*, 655, 345
- Lamzin, S., 1998, *ARep*, 42, 630
- Mundt, R., Bruegel, E.W., Buehrke, T., 1987, *ApJ*, 319, 275
- Muzerolle, J., Calvet, N., Hartmann, L., D'Alessio, P., 2003, *ApJ*, 597, L149
- Penston, M.V., Lago, M.T.V.T., 1983, *MNRAS*, 276, 203
- Preibisch, T., 2004, *ApSS*, 292, 631
- Romanova, M.M., Ustyugova, G.V., Koldoba, A.V., Lovelace, R.V.E., 2002, *ApJ*, 578, 420
- Schwartz, R.D., 1983, *ARA&A*, 21, 206
- Stempels, H.C., Piskunov, N., 2002, *A&A*, 391, 595
- Stempels, H.C., Gahm, G.F., Petrov, P.P., 2007, *A&A*, 461, 253
- Takami, M., Bailey, J., Gledhill, T. M., Chrysostomou, A., Hough, J. H, 2001, *MNRAS*, 323, 177
- von Rekowski, B., Brandenburg, A., 2004, *A&A*, 420, 17
- von Rekowski, B., Brandenburg, A., 2006, *AN*, 327, 53

**APPENDIX A: ATOMIC PARAMETERS FOR
THE CALCULATION OF THE LINE
EMISSIVITIES**

Table A1. Atomic parameters of the semiforbidden lines

Element	Wavelength $\lambda_{j,m}(\text{\AA})$	j	m	$A_{j,m}$ s^{-1}	w_j	Type ⁽¹⁾	$C^{(2)}$	$\langle \Upsilon_{j,m} \rangle^{(3)}$				
								0.0	0.25	0.50	0.75	1.00
Si III	1892.033	3	1	1.544×10^4	3	2	0.4	2.931	1.655	1.063	0.4002	0
C III	1908.737	3	1	97.32	3	2	1.1	0.3688	0.3419	0.3047	0.2102	0.0888

¹ Transition type according to Burgess & Tully (1992) classification. Type 2 includes transitions which are induced by either an electric multipole or a magnetic multipole, e.g. forbidden transitions.

^{2,3} Collisional rates have been computed following Burgess & Tully (1992). Thermally averaged collision strengths, $\langle \Upsilon_{j,m} \rangle(x)$, are given by interpolation for each temperature, T_e , using the coefficients indicated in the table with $x(T_e) = (k_B T_e / E_{j,m}) / (C + (k_B T_e / E_{j,m}))$ and $E_{j,m} = hc / \lambda_{j,m}$. The collision rate is: $8.6233 \times 10^{-6} n_e T_e^{-1/2} \langle \Upsilon_{j,m} \rangle / w_j$. (k_B : Boltzman constant; h : Planck constant; c : speed of light; w_j : statistical weight of level j .)